nanomaterials

MDPI

Article

Controlling the Oxidation of Magnetic and Electrically Conductive Solid-Solution Iron-Rhodium Nanoparticles Synthesized by Laser Ablation in Liquids

Ruksan Nadarajah [1], Shabbir Tahir [1], Joachim Landers [2], David Koch [3], Anna S. Semisalova [2], Jonas Wiemeler [2], Ayman El-Zoka [4], Se-Ho Kim [4], Detlef Utzat [2], Rolf Möller [2], Baptiste Gault [4,5], Heiko Wende [2], Michael Farle [2] and Bilal Gökce [1,*]

1 Technical Chemistry I and Center for Nanointegration Duisburg-Essen (CENIDE), University of Duisburg-Essen, Universitaetsstr. 7, 45141 Essen, Germany; ruksan.nadarajah@uni-due.de (R.N.); shabbir.tahir@uni-due.de (S.T.)

2 Faculty of Physics and Center for Nanointegration Duisburg-Essen (CENIDE), University of Duisburg-Essen, Lotharstr. 1, 47057 Duisburg, Germany; joachim.landers@uni-due.de (J.L.); anna.semisalova@uni-due.de (A.S.S.); jonas.wiemeler@uni-due.de (J.W.); detlef.utzat@uni-due.de (D.U.); rolf.moeller@uni-due.de (R.M.); heiko.wende@uni-due.de (H.W.); michael.farle@uni-due.de (M.F.)

3 Institute of Materials Science, University of Technology, Alarich-Weiss-Strasse 2, 64287 Darmstadt, Germany; david.koch@tu-darmstadt.de

4 Max-Planck-Institut für Eisenforschung GmbH, Max-Planck-Strasse 1, 40237 Düsseldorf, Germany; a.elzoka@mpie.de (A.E.-Z.); s.kim@mpie.de (S.-H.K.); b.gault@mpie.de (B.G.)

5 Department of Materials, Royal School of Mines, Imperial College London, London SW7 2AZ, UK

* Correspondence: bilal.goekce@uni-due.de; Tel.: +49-201-183-3146

Received: 23 October 2020; Accepted: 23 November 2020; Published: 27 November 2020

Abstract: This study focuses on the synthesis of FeRh nanoparticles via pulsed laser ablation in liquid and on controlling the oxidation of the synthesized nanoparticles. Formation of monomodal γ-FeRh nanoparticles was confirmed by transmission electron microscopy (TEM) and their composition confirmed by atom probe tomography (APT). For these particles, three major contributors to oxidation were analysed: (1) dissolved oxygen in the organic solvents, (2) the bound oxygen in the solvent and (3) oxygen in the atmosphere above the solvent. The decrease of oxidation for optimized ablation conditions was confirmed through energy-dispersive X-ray (EDX) and Mössbauer spectroscopy. Furthermore, the time dependence of oxidation was monitored for dried FeRh nanoparticles powders using ferromagnetic resonance spectroscopy (FMR). By magnetophoretic separation, B2-FeRh nanoparticles could be extracted from the solution and characteristic differences of nanostrand formation between γ-FeRh and B2-FeRh nanoparticles were observed.

Keywords: FeRh; nanoparticles; oxidation; laser ablation in liquid; FMR; Mössbauer; atom probe tomography; nanostrand

1. Introduction

Magnetic alloy nanoparticles offer a broad range of applications in catalysis [1–3], biomedicine [4–6], magnonics [7], and information technology [8,9]. Many applications require a colloidal form of the particles in water, organic solvents, or in polymer solutions for nanoparticle-polymer composites [10,11]. These nanoparticles can be synthesised by various bottom-up and top-down approaches such as chemical precipitation [12,13], solvothermal [14,15], solution-phase [16,17], and ball milling [18]. Laser ablation in liquids (LAL) is Therefore.

LAL is universally considered to be a physiochemical combined top-down (macroscopic solid targets) and bottom-up (initially formed plasma, atoms, and clusters) method, which needs no stabilizers or precursors to produce colloidal nanoparticles [19]. It has been proven to be a scalable method and a versatile process [20,21] due to the free choice of the target material and solvent [20]. Often LAL leads to the formation of oxides or metal complexes during ablation of metals. Even though magnetic metal oxide nanoparticles are omnipresent in science and technology, also metallic magnetic nanoparticles are needed for many applications for use in magnetic composites [22] or catalysis [23]. Hence, in this study we want to explore ways of minimizing the oxidation level of magnetic metal nanoparticles.

A challenging material in terms of oxidation is $Fe_{50}Rh_{50}$, which forms a body-centred cubic (bcc) structure known for its first order antiferro-ferromagnetic (AFM-FM) transition at T = 370 K [24]. This transition takes place near the equimolar ratio of FeRh with a lattice expansion of about 1%, an increase in entropy and net magnetic moment, and a decrease in electrical resistivity. A further magnetic phase transition occurs at the Curie temperature T_C = 650 K from the ferromagnetic to the paramagnetic phase. Since the discovery of $Fe_{50}Rh_{50}$ and its first-order phase transition, the system has extensively been investigated by many groups. The material changes its entropy when a magnetic field is applied which results in a thermal response (i.e., the magnetocaloric effect). Applications of this material can be found in areas such as heat-assisted magnetic recording [25,26], magnetocaloric cooling systems [27,28], (bio-)hyperthermia [29,30], and catalysis [31,32]. The phase transition temperature is known to be very sensitive to compositional changes near the equiatomic ratio [33].

Reports on the synthesis of FeRh nanoparticles can be found in the literature. Typically, wet chemical synthesis routes are used to produce nanoparticles for magnetic and catalytic applications [31,34,35]. In the field of catalysis, FeRh nanoparticles can reduce olefins and nitroarenes and also promote the conversion of syngas to C^{2+} oxygenates [1,31]. For many applications such as magnetic refrigeration, a composition near the equimolar composition is important e.g., to attain an AFM-FM transition at higher temperatures. The composition control of nanoparticles, however, is difficult using wet chemical approaches. In all cases using wet-chemistry, the synthesis of FeRh leads to the formation of core-shell NPs [35] or an alloy with inhomogeneous composition [36]. In addition, these FeRh nanoparticles have particle sizes smaller than 20 nm. And due to the high surface to volume ratio, these smaller nanoparticles are more prone to oxidation [34,36,37].

Since the properties of these alloys are sensitive to the change of composition, the control of oxidation becomes very important. Oxides have often different properties in terms of magnetism, catalytic activity, and electric/thermal conductivity than their metal counterparts [38,39]. The effects of synthetic environment on oxidation of iron-based alloys, e.g., FePt [40], FeAu [41,42], FeAg [43], was observed by varying one of the parameters. Amendola et al. found an influence of the solvent on the oxidation [44], while Marzun et al. pointed out the importance of molecular oxygen dissolved in the solvent [45]. However, a clear distinguishable contribution of the synthetic environment to oxidation, during LAL, is still outstanding. In the laser ablation process in general, the formed particles and the target are in an environment containing oxygen, which will inevitably lead to oxidation. Here, we report on the control and minimization of the oxidation of FeRh alloy nanoparticles by reducing possible oxidation sources during the laser ablation process in liquid.

2. Materials and Methods

In Figure 1, a schematic illustration of the experimental setup is shown. The laser pulse interacts with the target and creates a plasma plume, which consists of ionized and atomized species. During the plasma decay, the energy is transferred to the surrounding liquid which will evaporate and form a cavitation bubble, in which the nanoparticles are formed. The ablation is performed in a Schlenk-like ablation chamber, which allows the ablation in different atmospheres. Besides air, argon as an inert gas, and a mixture of 95% nitrogen and 5% hydrogen as a reducing gas was used to minimize the oxidation of the synthesized nanoparticles by preventing the exchange of oxygen from the atmosphere into the liquid. The chamber consists of two parts. The top part was built with a three-way valve for gas-flow

control. The lower part, where the ablation takes place, is made of a quartz glass cuvette (path length 0.5 cm) which is transparent for the laser wavelength of 1064 nm. More information about this setup can be found elsewhere [45].

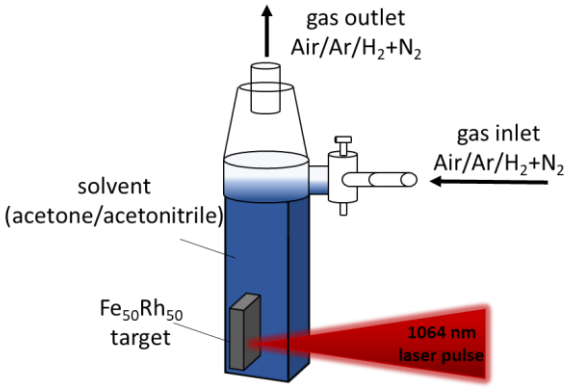

Figure 1. Schematic illustration of the "Schlenk" ablation chamber. The figure displays the laser setup and the different configurations with respect to solvents (acetone or acetonitrile) and gas flow. The gas inlet allows the manipulation of the atmosphere, with air, argon and a mixture of nitrogen and hydrogen. A laser with a pulse duration of 10 ps, repetition rate of 100 kHz and wavelength of 1064 nm was used.

Here, LAL was performed in an organic solvent (acetone, acetonitrile) using a picosecond pulsed Nd-YAG laser (Ekspla, Atlantic Series, Vilnius, Lithuania, 10 ps, 100 kHz, 80 µJ, 1064 nm). The laser beam was directed into a laser scanner and focused by an f-theta lens (focal length of 100.1 mm). The laser beam has a Gaussian profile with a laser fluence of 3.5 J/cm^2. A scanning speed of 6 m/s was chosen, to spatially bypass the laser-induced cavitation bubbles and neglect the influence of the scanning speed [46]. The particle morphology, composition, and size distribution were analysed by transmission electron microscopy (TEM) (JEOL 2200FS, Freising, Germany) and atom probe tomography (APT) (Cameca 5076XS, Gennevilliers Cedex, France). Phase analysis was conducted by X-ray diffraction (XRD). The XRD measurements were performed using Mo Kα radiation in transmission geometry on a custom-built setup with a Mythen2 R 1K detector (Dectris Ltd., Baden, Switzerland). The sample was mixed with NIST 640d standard silicon powder for correcting geometric errors and glued on a graphite foil. Energy-dispersive X-ray spectroscopy (EDX) in the dried form and Mössbauer spectroscopy on colloidal samples were conducted to test the oxidation level and to characterize the particles' structural and magnetic properties. Mössbauer spectra were taken in transmission geometry and constant acceleration mode at 4.3 K and ca. 80 K using a l-He bath cryostat. The ferromagnetic resonance (FMR) experiments were performed using a Bruker Elexsys E500 EPR spectrometer in the X-band (9.5 GHz) via conventional cavity-based FMR detection. The observed signal is proportional to the B-field derivative of the imaginary part of magnetic susceptibility, $\partial\chi''/\partial B$. Time-dependent FMR measurements were performed to study the effect of oxidation on the resonance field and lineshape of the FeRh nanoparticles. A small amount of the solution (0.013 mL) containing the nanoparticles in acetone was filled into a quartz tube (2 mm ID)/

To fabricate APT specimens, freestanding nanoparticles first were encapsulated. The as-synthesized FeRh nanoparticles were originally suspended in acetone. To remove the acetone, the suspension was left to dry in a nitrogen glovebox. The collected nanoparticles were co-electrodeposited with Ni according to the protocol detailed in ref [47]. The dried FeRh NP powder was dispersed in a Ni ion electrolyte followed by pouring the solution into a vertical electro-cell where a counter electrode (Pt mesh) positioned on top and a working electrode (Cu foil) placed at the bottom. A low constant current (−19 mA) was applied to the electrodes to co-electrodeposit Ni and NPs on the working electrode. After the deposition, the composite film was kept in a vacuum desiccator.

The electroplated composite film was loaded into the focused ion beam (FIB) (Helios 600, Fei, OR, USA) and needle-shaped specimens were prepared following the in-situ lift-out protocol outlined in ref. [48]. APT measurements were done using a UV-laser assisted LEAPTM 5000 XS system (CAMECA Instruments Inc., Gennevilliers Cedex, France). at an analysis stage temperature of 40 K. The laser repetition rate was set to 200 kHz, and the laser pulse energy was 60 pJ. Data was acquired with a detection rate of 5 ions for 1000 pulses on average. Multiple datasets containing over 15 million ions were collected. Data analyses were performed using the commercial software, IVAS 3.8.4.

Furthermore, nanostrands were formed by producing a solution of 5 wt% poly(methylmethacrylate) (PMMA) with 0.2 wt% FeRh NPs in acetone. The solution was dried on a glass substrate in an external magnetic field, with a flux density of 150 mT. The dried sample with the formed nanostrands was imaged using an optical microscope (CX 40, Olympus, Tokyo, Japan). More information on the setup and formation mechanism can be found elsewhere [10]. The conductivity of the nanostrands was measured by using thin-film gold interdigitated electrodes (Micrux, Gijón, Spain).

The ablation target was custom-made by the "Research Institute for Noble Metals and Metal Chemistry", Schwaebisch Gmuend, Germany and has an equimolar composition (±1.5%) according to X-ray fluorescence (XRF) and energy-dispersive X-ray (EDX) measurements.

3. Results and Discussion

To minimize oxidation of the alloy nanoparticles, 3 major contributors to oxidation were analysed. (1) Dissolved oxygen in the organic solvents, (2) bound oxygen in the solvent due to the dissociation of the solvent during the LAL process [49] and (3) oxygen in the air. To study the influence of bound oxygen, acetone and acetonitrile were used as solvents. Both are similar organic solvents with the difference that acetone has bound oxygen while acetonitrile contains nitrogen instead. Both solvents were successfully used in the literature to synthesize elemental metal nanoparticles [45,50].

Figure 2a shows the number-weighted size distribution of $Fe_{50}Rh_{50}$ nanoparticles synthesized in acetone and acetonitrile under argon atmosphere. The size distribution can be fitted using a lognormal function, which leads to a mean particle size of 16.44 ± 6.67 nm (acetone, red) and 15.48 ± 5.93 nm (acetonitrile, blue), respectively. With a polydispersity index (PDI) lower than 0.3, both particle size distributions can be considered as monomodal. Nanoparticle productivities of 43.6 mg/h and 41.2 mg/h were reached in acetone and acetonitrile, respectively. XRD measurements (Figure 2b) of the particles in acetone with argon atmosphere show that there is almost no visible B2 phase, which corresponds to the α'-FeRh phase (bcc), which is antiferromagnetic at room temperature, as we would expect from bulk FeRh near the equimolar ratio. Instead, almost all the particles are in the γ-phase, which was also found by Jia Z. et al. for FeRh nanoparticles of 4–20 nm size synthesized by a polyol coreduction process [34]. Rietveld refinement via the "Fullprof" software [51] shows that almost all FeRh nanoparticles are in the γ-phase, with a lattice parameter of 3.81 Å. The formation of the γ-phase is also supported by density functional theory calculations [52] which showed that due to the similar energy states of AFM/BCC FeRh and metastable FCC FeRh epitaxial strain can easily transform the BCC to the FCC structure.

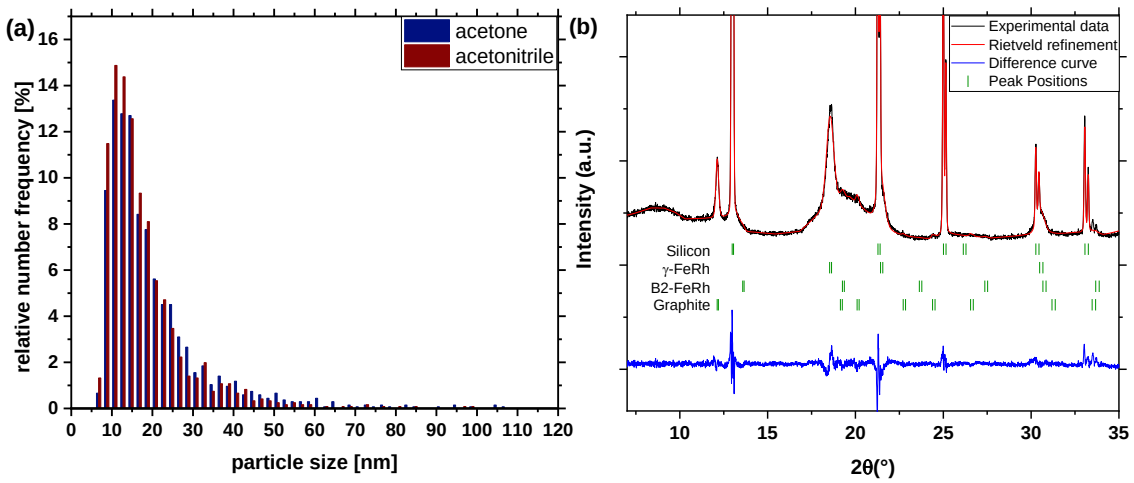

Figure 2. (**a**) Number-weighted particle size distribution (extracted from TEM images) of synthesized particles by laser ablation in acetone and acetonitrile and (**b**) XRD-pattern of $Fe_{50}Rh_{50}$ nanoparticles obtained by laser ablation in acetone and acetonitrile. The known XRD peaks of γ—FeRh, graphite and B2-FeRh and silicon are indicated.

Figure 3a shows the EDX line scan for a representative particle which was synthesized in acetone under air atmosphere. The content of oxygen was found to be as high as 74.4 at% (37.9 wt%). Furthermore, an oxygen signal of areas without particles can be found. An unbound oxide layer could be originated due to pyrolysis of solvent molecules leading to the formation of amorphous organic by-products in the presence of water, which is avoided using molecular sieves, e.g., during the drying step on the TEM grids (Figure 3). Water is soluble in air, and at 25 °C, 1 m^3 of air can hold up to 22 g of water at 100% humidity. As water is miscible in acetone and is one of the main suppliers of oxygen, a mole sieve with a pore size of 3 Å was used to remove the water content in the acetone, which could have been transferred from the air to the solvent. A reduction of the detected oxygen from 74.4 at% (37.9 wt%) to 24.3 at% (6.0 wt%) can be observed in Figure 3. As water was found to be a major contributor for the oxidation, all further experiments were performed with a mole sieve purified solvent.

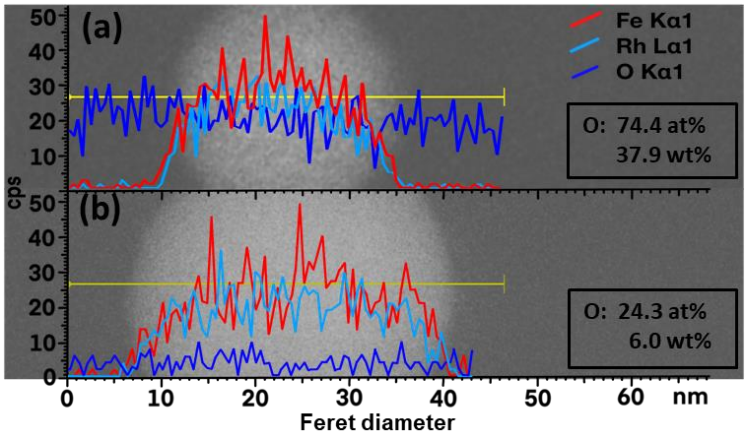

Figure 3. EDX line-scan of single $Fe_{50}Rh_{50}$ nanoparticles obtained by laser ablation in acetone (**a**) with the use of a mole sieve, and (**b**) without the use of a mole sieve.

The degree of oxidation of the synthesized iron-rhodium alloy nanoparticles was further examined in acetone and acetonitrile. As the surrounding atmosphere is also a potential oxygen supplier for oxidation, the ablation was conducted in 3 different atmospheres. As an atmosphere, besides air as a reference, argon was chosen as an inert gas. Further, the process was tested with a mixture of

nitrogen and hydrogen as a reduction gas, which will eventually reduce the formed oxidation. Figure 4 summarizes EDX line scans for individual FeRh nanoparticles obtained for all configurations presented in the Table 1. The particle size can have an impact on the oxidation, therefore particles of similar size of ~30 nm were chosen to have comparable results. Furthermore, too small particles will result in a poor signal-to-noise ratio. As smaller particles have a higher surface-to-volume ratio and the oxide level of the smaller particles can therefore be much higher in comparison, EDX is used as a screening method and selected particles are further analysed by atom probe tomography (APT) and Mössbauer spectroscopy.

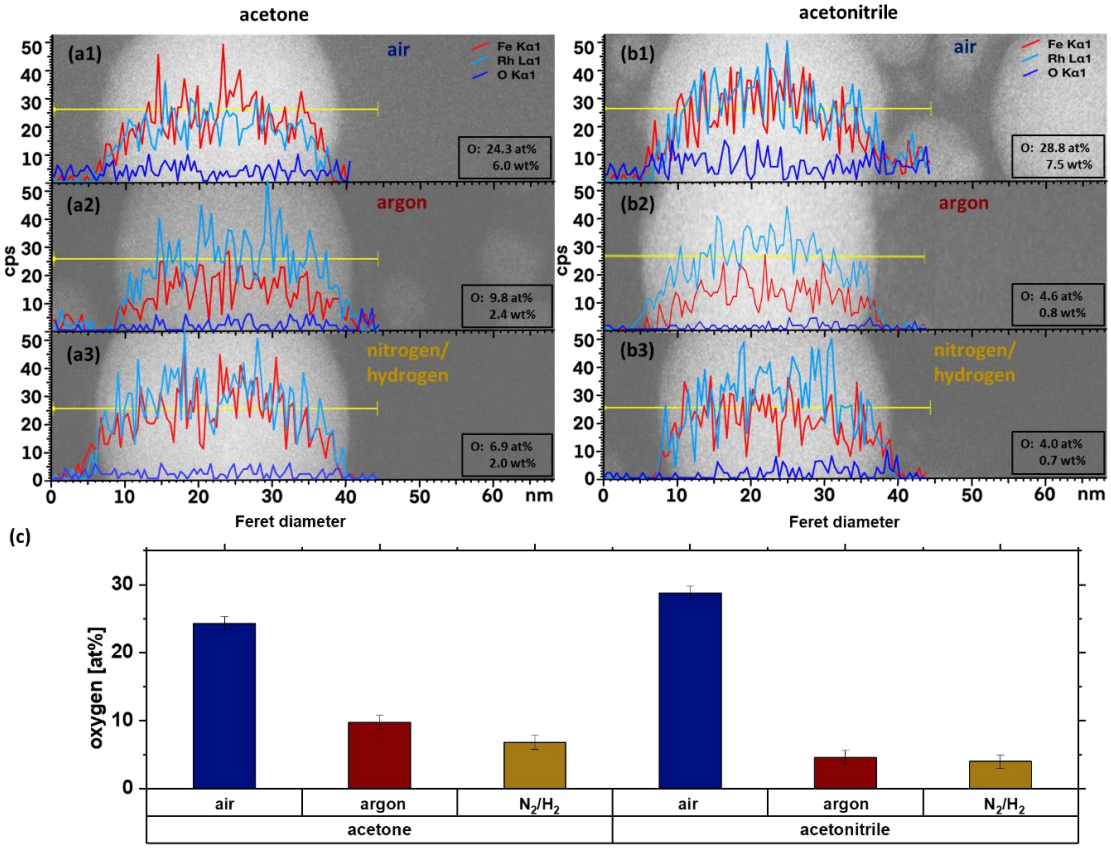

Figure 4. EDX line-scan of $Fe_{50}Rh_{50}$ nanoparticles synthesized in acetone under (**a1**) air, (**a2**) argon, (**a3**) N_2/H_2 mixture atmosphere and in acetonitrile under (**b1**) air, (**b2**) argon, (**b3**) N_2/H_2 mixture atmosphere. Panel (**c**) depicts the extracted oxygen fraction for the different configurations.

Table 1. Configuration of solvent and atmosphere during LAL.

Configuration	Solvent	Atmosphere
a1	acetone	air
a2	acetone	argon
a3	acetone	N_2/H_2
b1	acetonitrile	air
b2	acetonitrile	argon
b3	acetonitrile	N_2/H_2

As seen in Figure 4a, the EDX-line scan of the particles which were ablated in acetone under the air atmosphere showed an oxide level of 24.3 at%. When argon or the N_2/H_2 mixture was used as an atmosphere, the detected oxygen was reduced to 9.8 at% and 6.9 at%, respectively. M. Quaranta et al. calculated that the solubility of oxygen in acetone and acetonitrile is 2.55 ± 0.19 mM and 2.60 ± 0.15 mM, respectively [44]. This means that the proportion of oxygen, which promotes oxidation in the solvent,

is the same for both solvents. As the amount of dissolved oxygen in the solution is the same, the change of oxidation would be solely due to bound oxygen in the acetone molecule. An effect of the bound oxygen could not be observed.

For more advanced characterization of the elemental distribution within the nanoparticles, we performed APT analysis on FeRh nanoparticles after electrochemical embedding in Ni (see Materials and Methods). Figure 5a shows a 3D atom map of Fe-Rh nanoparticles with representative sizes and respective chemical profiles in Ni deposit. The particle surface is highlighted using a set of iso-composition surfaces encompassing regions containing more than 10 at% (Fe + Rh). Interestingly, the APT analysis of FeRh nanoparticles shows the homogenous distribution of Fe and Rh across the nanoparticles with different sizes (Figure 5 and Figure S1), which is in contrast to known literature, where only core-shell particles were reported [35–37,53]. The acquired particle in Figure 5b has a higher composition of Fe while another particle shows the opposite with a higher Rh composition (see Supplementary Figure S1). No oxygen could be detected in the particle shown in Figure 5b.

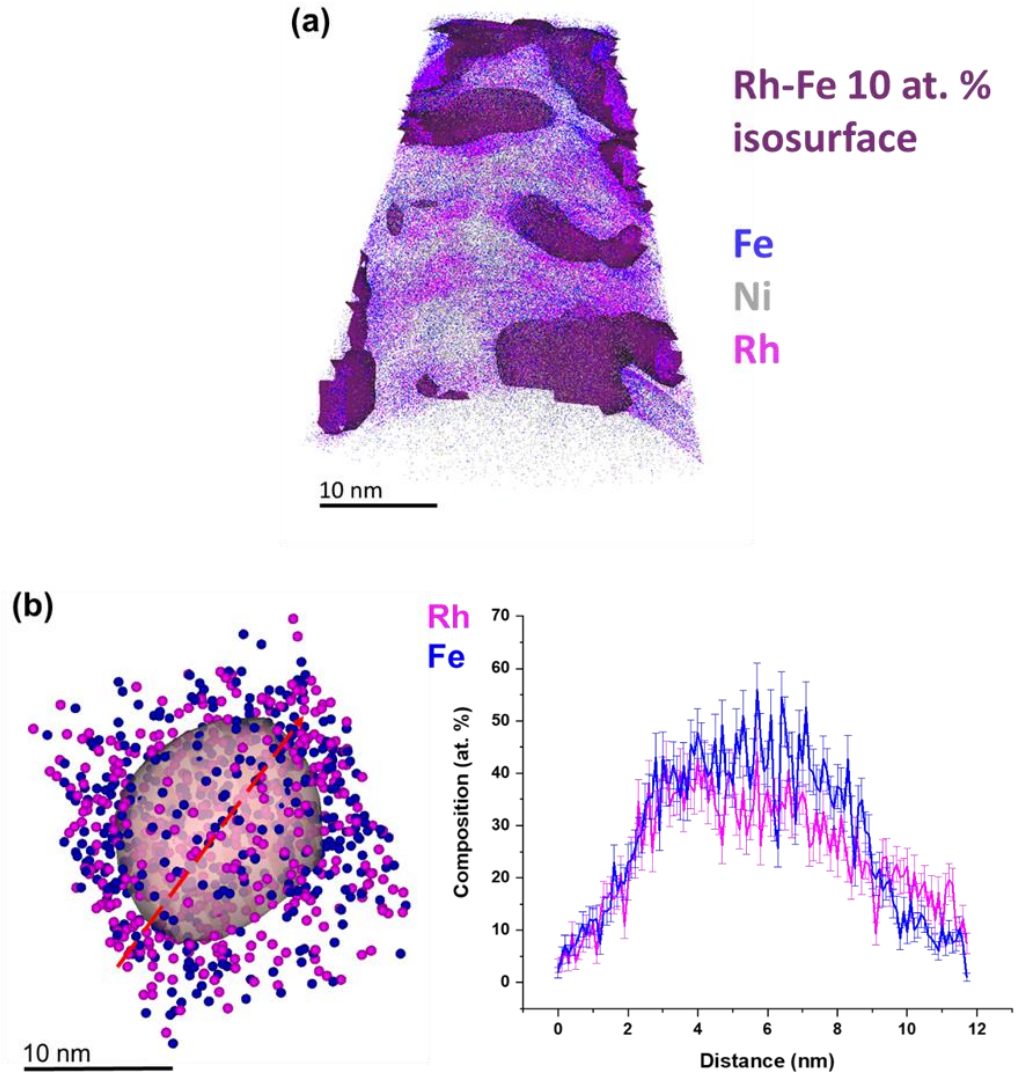

Figure 5. Atom probe tomography of FeRh nanoparticles synthesized in acetone and argon atmosphere. (**a**) 3D atom map of FeRh nanoparticles in Ni deposit. Blue, purple, and grey dots mark the reconstructed positions of Fe, Rh, and Ni, respectively. Detected FeRh nanoparticles are highlighted by 10 at% FeRh iso-composition surfaces. (**b**) Extracted FeRh nanoparticle (25 at% of FeRh iso-composition surface) and line scan of selected FeRh nanoparticle.

We further conducted an 1D compositional profile through a second (smaller) FeRh nanoparticle (Figure S1). Smaller particles are typically more prone to oxidation as also indicated by the residual oxygen content of up to approx. 9.6 at%, that was determined for this smaller particle. This may originate not only from nanoparticle synthesis but also from the APT sample preparation, for which an aqueous electrolyte is used. Nevertheless, the levels of O detected inside the nanoparticle suggest the presence of oxygen inside the small nanoparticles (Figure S1) and no detectable oxygen inside the bigger nanoparticle (Figure 5).

In Figure 4, EDX was used as a screening method. As Mössbauer spectroscopy has the ability to directly distinguish metal and oxide constituents, it is used here to verify the EDX findings. To compare the results of both techniques, it also has to be considered that particles were measured in the dried state in EDX and in solution via Mössbauer spectroscopy and that the latter provides an integral signal averaged over the whole sample, unlike single particle analysis as done in EDX or APT. To allow measurements of the particles in solution, Mössbauer spectra as shown in Figure 6 were recorded using a liquid-tight screw-mountable sample holder at 4.3 K and 79 K for samples prepared in acetone and acetonitrile in atmospheres of air and argon, respectively.

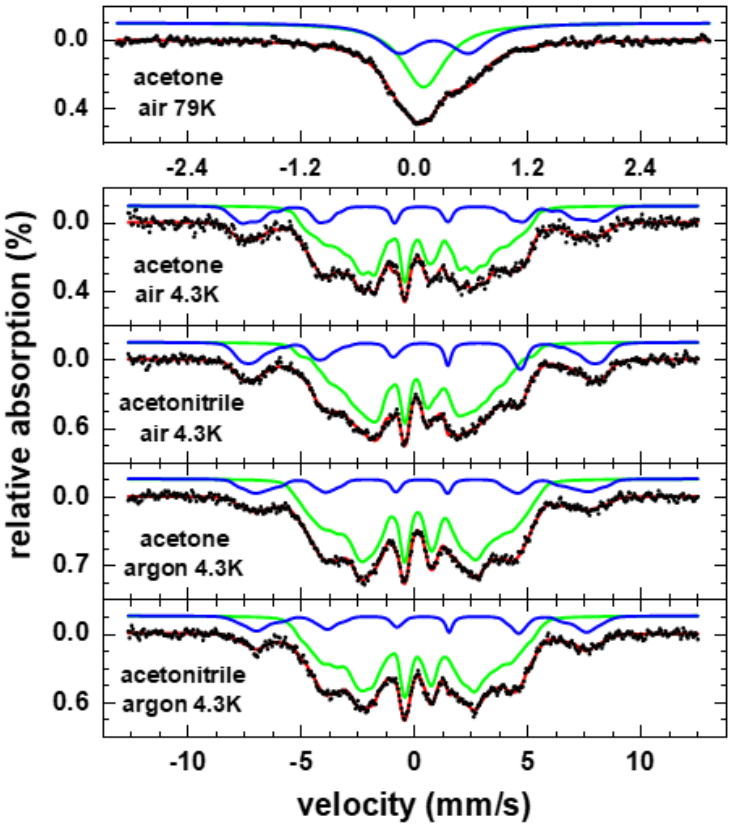

Figure 6. Mössbauer spectra of laser ablated FeRh nanoparticles in solution prepared under air/argon atmosphere in acetone or acetonitrile, respectively. Spectra were recorded at 4.3 K; subspectra can be assigned to metallic γ-phase FeRh (green) and an Fe^{3+}-oxide phase (blue). A spectrum obtained at 79 K is shown for comparison on top.

At 4.3 K, we observe two magnetically ordered sextets, which can be assigned to metallic FeRh (green curve in Figure 6) and presumably a Fe^{3+}-oxide state based on their different average hyperfine magnetic fields of ca. 21 and 45.5 T and isomer shifts of ca. 0.29 and 0.45 mm/s relative to α-Fe at room temperature, respectively. Instead of narrow absorption lines, both subspectra are distinctly broadened, wherefore they were reproduced via distributions of hyperfine magnetic fields. For the oxide phase, this broadening could potentially be explained by being present as an amorphous oxide

surface layer, hindering an in-detail analysis of this phase's spectral properties. For the metallic constituent, on the other hand, the observed distribution is in agreement with previous reports on antiferromagnetic γ-phase FeRh, although average hyperfine magnetic fields are somewhat higher here in comparison, which could be connected e.g., to minor variations in local stoichiometry or strain effects in the nanoparticles [54,55]. The presence of γ-FeRh in particles studied here is also supported by the absence of magnetic ordering in the reference spectrum recorded at 79 K, consistent with the low ordering temperature of γ-FeRh [55], although in theory, superparamagnetic relaxation of smaller FeRh nanoparticles could also contribute to the doublet present at this temperature. The higher superposition of subspectra at 79 K prevents a precise estimation of metallic and oxide fraction, while at 4.3 K similar oxide fractions of ca. 16% and 21% are found for the sample prepared in argon and air, respectively (see also Table 2), relatively independent of the used solvent. Assuming identical Lamb-Mössbauer factors for both components at 4.3 K, relative spectral areas as given here correspond in good approximation to the fraction of Fe-atoms in the respective phase (Table 2), in general yielding similar trends as EDX-analysis in terms of nanoparticle oxidation.

Table 2. Oxide fractions extracted from the Mössbauer spectra (fraction of Fe-atoms in the oxide phase).

	Acetone	*Acetonitrile*
air	20.3 ± 1.7 at%	21.5 ± 1.9 at%
argon	15.7 ± 1.6 at%	15.9 ± 1.4 at%

Ablation in acetone and acetonitrile shows the same amount of oxide and corresponds to the EDX-measurements in Figure 4, while the influence of the bound oxygen of the acetone molecule cannot be seen in the Mössbauer spectra. Furthermore, the ablation in air shows 20–22 at% of oxidation, while the ablation in the argon atmosphere results in an oxide content of 15–16 at%. Although the trend is the same as in the EDX line scans, it is difficult to compare absolute numbers determined by both methods: EDX provides atomic fraction of O-atoms, whereas Mössbauer spectroscopy provides the fraction of Fe-atoms, which are part of the oxide phase. Smaller particles, which cannot be measured with EDX, can have a higher degree of oxidation, and would also contribute to the oxide fraction extracted from Mössbauer spectra.

To probe the magnetization of the FeRh particles and to monitor the time dependent oxidation of the dried FeRh particles in air, ferromagnetic resonance measurements were conducted. Based on the EDX and Mössbauer spectroscopy results, we chose particles which were synthesized in acetone and argon atmosphere as this configuration was expected to lead to a minimum of oxidation.

In Figure 7, a typical FMR spectrum is shown. The spectrum of FeRh NPs in acetone was found to have an asymmetric lineshape, which is typical for an ensemble of ferromagnetic nanoparticles—the observed line is the sum of multiple FMR Lorentz-shape spectra from individual nanoparticles varying in size, shape, and orientation of the anisotropy axes [56,57]. The FMR signal is proportional to the magnitude of the magnetization of the sample [58]. The resonance field is a measure of the internal magnetic field which consists of shape and magnetocrystalline anisotropy fields and includes possible dipolar coupling effects between particles. The peak-to-peak linewidth of the FMR spectrum of the nanoparticles ensemble reflects the distribution of magnetic anisotropy axes, as well as the size distribution, being practically insensitive to the concentration of magnetic fraction [59–61], if dipolar interactions are not dominant.

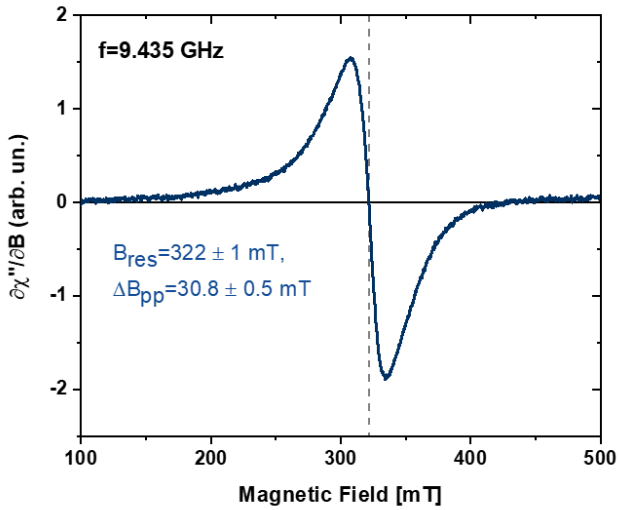

Figure 7. The ferromagnetic resonance spectrum measured at 9.435 GHz of a FeRh nanoparticles solution in acetone at room temperature. B_{res} is the resonance field (dotted line), ΔB_{pp} is the peak-to-peak linewidth.

The total magnetic anisotropy of nanoparticles given by a combination of shape, magnetocrystalline, including surface anisotropy contributions, has been shown to be effectively describable by a uniaxial anisotropy field $B_A = \frac{2K_{eff}}{M_s}$, where K_{eff} is the effective anisotropy constant and M_s is the saturation magnetization. The resonance field value B_{res} = 322 ± 1 mT observed for the ensemble of FeRh nanoparticles in acetone (Figure 7) can be analysed within the model of randomly distributed easy axes of magnetization [62]. In this model, the measured resonance field is shifted to lower values from the resonance field for zero anisotropy. Assuming the g-factor for $Fe_{50}Rh_{50}$ nanoparticles g = 2.05 ± 0.02 [53,63] corresponding to an isotropic resonance field $B_0 = \frac{h\nu}{g\mu_B} = 330 \pm 3$ mT, one obtains a small anisotropy field B_A = 47 ± 10 mT at room temperature.

The evolution of the FMR signal was monitored on the dried FeRh nanoparticles exposed to a mixture of air and solvent vapour over 46 h. During the first 6 h, the FMR absorption spectra were recorded every hour. Few exemplary spectra are shown in Figure 8a. Figure 8b presents the time evolution of the resonance field and peak-to-peak linewidth. The resonance field increases with time, approaching a saturation value of 324.9 ± 0.2 mT after 6 h, a similar change and saturation can be seen for the linewidth, which increases from 30.8 ± 0.5 mT for nanoparticles in solution, to 41.5 ± 0.4 mT for dried nanoparticles within the first 10 h after removal of acetone. This shift of the resonance field towards the isotropic value indicates a decrease of the effective anisotropy field driven by surface oxidation. Here, we like to note that due to the experimental arrangement "oxidation" does not necessarily refer to the presence of oxygen but may also be due to electron transfer to chemisorbed surface ligands. The change of the resonance field can be attributed to the change of surface anisotropy, strain effects due to the lattice mismatch of oxidized and non-oxidized FeRh as well as reduction of ferromagnetic volume of the particle. The relative role of these effects can be distinguished using magnetometry, FMR and additional techniques (for example, EDX and high-resolution transmission electron microscopy) on the series of samples with varying size and oxidation degree. The detailed study of surface anisotropy contribution and strain due to lattice mismatch between oxidized and non-oxidized FeRh can be performed with temperature-dependent as well as microresonator FMR technique. The oxidation of the particles takes place within the first 6–10 h after removal of acetone until a passivating layer is formed, similar to the one observed in $Fe_{50}Rh_{50}$ thin films [64]. Further studies of magnetization dynamics in array of nanoparticles including mapping of microwave excitations in the particles of different size are possible using spatially resolved FMR as well as Brillouin light scattering (BLS) [65–67].

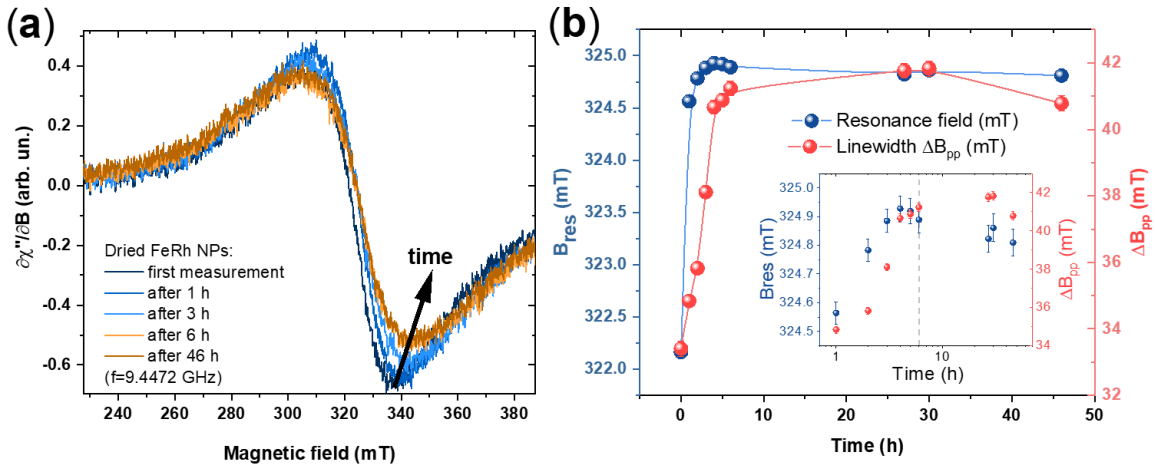

Figure 8. (**a**) Evolution of FMR spectra for $Fe_{50}Rh_{50}$ nanoparticles during 46 h after drying; (**b**) time dependence of the corresponding resonance field and linewidth. Inset shows the data in logarithmic time scale, dot line marks 6 h.

As an outlook for future applications, these particles with minimized oxidation are used for nanostrand formation in a transparent polymer (Figure 9) to combine the magnetic response and the electrical conductivity of the nanoalloy to tune the electrical conductivity of the polymer [11,68]. These composites could potentially be used as a window coating for electric heating while being transparent in the optical range [10]. As most of the particles are in the γ-phase, the magnetic response of the $Fe_{50}Rh_{50}$ nanoparticles can be shown, through the magnetic separation of the B2-phase. FeRh nano-strands are formed by applying a magnetic field (150 mT) during the formation of PMMA-FeRh composites, which is depicted in Figure 9. Due to the external magnetic field, the NPs are magnetized and exhibit a local magnetic field, resulting in the attraction of the particles and alignment to strands. As most of the prepared $Fe_{50}Rh_{50}$ nanoparticles in the colloid are in γ-phase, which is paramagnetic at room temperature, the magnetization is too weak to form nano-strands. As the Rietveld refinement (Figure 2b) shows no clear B2-phase of the sample, magnetic separation was conducted, to separate the magnetic fraction. These separated particles led to strand formation (Figure 9b), with maximum strand lengths of 9.5 µm, which indicates a higher magnetization, comparable to ferromagnetic materials (B2-phase). An average nanostrand length of 2.6 ± 1.2 µm was observed.

The FeRh nanoparticles were further tested in terms of conductivity. Therefore, the colloid was drop casted on an interdigital electrode without the polymer. Figure 9d shows that the electrode without strands exhibits a lower output voltage than the sample with the formed nanostrands on the electrodes. If we account for the series of resistance (shunt) of the setting, the voltage drop on this shunt yields the current. The current on the electrode without nanostrands is 95.5 nA, whereas the current of the electrode with the formed strands is 0.85 mA, which is almost a factor of 9000 higher.

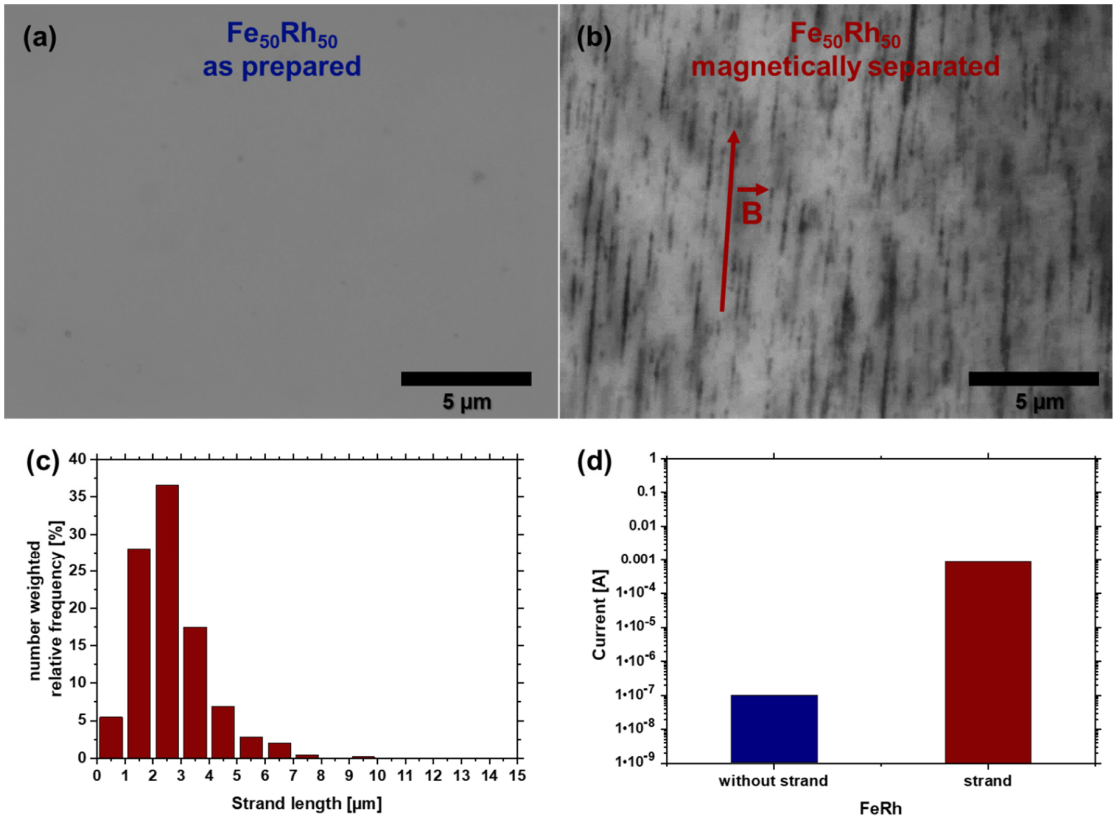

Figure 9. Magnetic-field induced FeRh nanostrand formation in a polymer. Light optical microscopy images of the composite containing $Fe_{50}Rh_{50}$ nanostrands from (**a**) as-prepared nanoparticles and (**b**) after magnetic separation. The red arrow denotes the direction of the magnetic field. (**c**) Quantification of nanostrand length as extracted from microscopy through image analysis. (**d**) Conductivity measurement of the FeRh particles without and with formed FeRh nanostrands.

4. Conclusions

Laser ablation in liquid was successfully applied to synthesize metallic solid solution FeRh nanoparticles. The produced particles have monomodal size distribution with a PDI lower than 0.3 and a mean particle size of 15.24 nm for acetone and 14.46 nm for acetonitrile, respectively. Atom probe tomography confirmed the formation of solid solution FeRh nanoparticles. Three different kinds of oxygen sources were determined and analysed. It was found that residual water in the organic solvent leads to high oxidation of the particles, which was reduced by up to 50% by using a mole sieve to 24.3 at% detected oxygen in the sample. Choosing an inert or reduction gas such as argon or hydrogen/nitrogen mixture can reduce the oxidation of the particles by an additional 5%. An impact of the bound oxygen in the molecule of the organic solvent could not be found. Furthermore, the oxidation behaviour after ablation in the dried state was studied by FMR, which showed a shift of the resonance field driven by surface oxidation in the first 6 h after drying and then saturate. To apply the oxidation-minimized nanoparticles in a polymer composite, conductive nanostrands with an average nanostrand length of 2.6 ± 1.2 µm were formed from the nanoparticles after magnetic separation. The strands after magnetic separation had a factor of 9000 higher current on the electrode than single particles without the PMMA compounds. As a potential application these transparent composite could be used as a window coating for rear window defroster. Our findings show that laser ablation in liquid is a feasible method to synthesize FeRh nanoparticle with a minimized oxidation level.

Supplementary Materials: The following are available online at http://www.mdpi.com/2079-4991/10/12/2362/s1, Figure S1: Atom probe tomography of FeRh nanoparticles synthesized in acetone and argon atmosphere. Extracted FeRh nanoparticle (25 at% of FeRh iso-composition surface) and line scan of selected FeRh nanoparticle.

Author Contributions: Investigation, R.N., S.T. and J.L.; data curation, R.N., D.K., A.S.S., J.W., A.E.-Z., S.-H.K. and D.U.; methodology R.N.; visualization R.N., J.L., D.K., A.S.S., A.E.-Z. and S.-H.K.; validation, R.N., J.L., D.K. and A.S.S.; writing—original draft, R.N.; writing—review & editing all authors; supervision R.M., B.G. (Baptiste Gault), H.W., M.F. and B.G. (Bilal Gökce); conceptualization M.F. and B.G. (Bilal Gökce), funding acquisition B.G. (Bilal Gökce). All authors have read and agreed to the published version of the manuscript.

Funding: The authors gratefully acknowledge the funding by the German Research Foundation (DFG) within the Collaborative Research Centre/Transregio (CRC/TRR) 270 (Project-ID 405553726, projects B04, B05, B08, B09 and Z01). Bilal Gökce further thanks the DFG for funding his projects GO 2566/2-1 and GO 2566/10-1. Ayman El-Zoka, Se-Ho Kim, and Baptiste Gault acknowledge financial support from the ERC-CoG-SHINE-771602.

Acknowledgments: We acknowledge support by the Open Access Publication Fund of the University of Duisburg-Essen. We thank Vaijayanthi Ramesh for her help with the TEM-image processing. We thank Soma Salamon and Benedikt Eggert for fruitful discussions on the interpretation of Mössbauer spectroscopy data.

Conflicts of Interest: The authors declare no conflict of interest.

References

1. Nakamula, I.; Yamanoi, Y.; Imaoka, T.; Yamamoto, K.; Nishihara, H. A Uniform Bimetallic Rhodium/Iron Nanoparticle Catalyst for the Hydrogenation of Olefins and Nitroarenes. *Angew. Chem. Int. Ed.* **2011**, *50*, 5830–5833. [CrossRef] [PubMed]
2. Elsayed, I.; Mashaly, M.; Eltaweel, F.; Jackson, M.A.; Hassan, E.B. Dehydration of glucose to 5-hydroxymethylfurfural by a core-shell Fe_3O_4@SiO_2-SO_3H magnetic nanoparticle catalyst. *Fuel* **2018**, *221*, 407–416. [CrossRef]
3. Yiu, H.H.P.; Keane, M.A. Enzyme-magnetic nanoparticle hybrids: New effective catalysts for the production of high value chemicals. *J. Chem. Technol. Biotechnol.* **2012**, *87*, 583–594. [CrossRef]
4. Wilhelm, C.; Gazeau, F. Universal cell labelling with anionic magnetic nanoparticles. *Biomaterials* **2008**, *29*, 3161–3174. [CrossRef] [PubMed]
5. Tran, N.; Webster, T.J. Nanotechnology for bone materials. *Wiley Interdiscip. Rev. Nanomed. Nanobiotechnol.* **2009**, *1*, 336–351. [CrossRef] [PubMed]
6. Sun, C.; Lee, J.S.; Zhang, M. Magnetic nanoparticles in MR imaging and drug delivery. *Adv. Drug Deliv. Rev.* **2008**, *60*, 1252–1265. [CrossRef] [PubMed]
7. Sadovnikov, A.V.; Grachev, A.A.; Gubanov, V.A.; Odintsov, S.A.; Martyshkin, A.A.; Sheshukova, S.E.; Sharaevskii, Y.P.; Nikitov, S.A. Spin-wave intermodal coupling in the interconnection of magnonic units. *Appl. Phys. Lett.* **2018**, *112*, 142402. [CrossRef]
8. Swisher, J.; Robbins, M.; Sherwood, R.; Fuchs, E.; Lockwood, W.; Keilp, J. Polymer-coated metal and alloy particles for magnetic recording. *IEEE Trans. Magn.* **1971**, *7*, 155–158. [CrossRef]
9. Zhang, H.-W.; Liu, Y.; Sun, S. Synthesis and assembly of magnetic nanoparticles for information and energy storage applications. *Front. Phys. China* **2010**, *5*, 347–356. [CrossRef]
10. Barcikowski, S.; Baranowski, T.; Durmus, Y.; Wiedwald, U.; Gökce, B. Solid solution magnetic FeNi nanostrand-polymer composites by connecting-coarsening assembly. *J. Mater. Chem. C* **2015**, *3*, 10699–10704. [CrossRef]
11. Beck, G.; Barcikowski, S.; Chakravadhanula, V.S.K.; Comesaña-Hermo, M.; Deng, M.; Farle, M.; Hilgendorff, M.; Jakobi, J.; Janek, J.; Kienle, L.; et al. An approach for transparent and electrically conducting coatings: A transparent plastic varnish with nanoparticulate magnetic additives. *Thin Solid Film.* **2015**, *595*, 96–107. [CrossRef]
12. Rashid, H.; Mansoor, M.A.; Haider, B.; Nasir, R.; Hamid, S.B.A.; Abdulrahman, A. Synthesis and characterization of magnetite nano particles with high selectivity using in-situ precipitation method. *Sep. Sci. Technol.* **2020**, *55*, 1207–1215. [CrossRef]
13. Khalil, M.I. Co-precipitation in aqueous solution synthesis of magnetite nanoparticles using iron(III) salts as precursors. *Arab. J. Chem.* **2015**, *8*, 279–284. [CrossRef]
14. Jamshidiyan, M.; Shirani, A.; Alahyarizadeh, G. Solvothermal synthesis and characterization of magnetic Fe_3O_4 nanoparticle by different sodium salt sources. *Mater. Sci.* **2017**, *35*, 50–57. [CrossRef]
15. Zhang, W.; Shen, F.; Hong, R. Solvothermal synthesis of magnetic Fe3O4 microparticles via self-assembly of Fe_3O_4 nanoparticles. *Particuology* **2011**, *9*, 179–186. [CrossRef]

16. Wu, L.; Mendoza-Garcia, A.; Li, Q.; Sun, S. Organic Phase Syntheses of Magnetic Nanoparticles and Their Applications. *Chem. Rev.* **2016**, *116*, 10473–10512. [CrossRef]
17. Shen, B.; Sun, S. Chemical Synthesis of Magnetic Nanoparticles for Permanent Magnet Applications. *Chemistry* **2020**, *26*, 6757–6766. [CrossRef]
18. De Carvalho, J.; Medeiros, S.N.; Morales, M.; Dantas, A.L.; Carriço, A. Synthesis of magnetite nanoparticles by high energy ball milling. *Appl. Surf. Sci.* **2013**, *275*, 84–87. [CrossRef]
19. Zhang, D.; Gökce, B.; Barcikowski, S. Laser Synthesis and Processing of Colloids: Fundamentals and Applications. *Chem. Rev.* **2017**, *117*, 3990–4103. [CrossRef]
20. Streubel, R.; Barcikowski, S.; Gokce, B. Continuous multigram nanoparticle synthesis by high-power, high-repetition-rate ultrafast laser ablation in liquids. *Opt. Lett.* **2016**, *41*, 1486–1489. [CrossRef]
21. Kohsakowski, S.; Santagata, A.; Dell'Aglio, M.; De Giacomo, A.; Barcikowski, S.; Wagener, P.; Gökce, B. High productive and continuous nanoparticle fabrication by laser ablation of a wire-target in a liquid jet. *Appl. Surf. Sci.* **2017**, *403*, 487–499. [CrossRef]
22. Jakobi, J.; Petersen, S.; Menéndez-Manjón, A.; Wagener, P.; Barcikowski, S. Magnetic Alloy Nanoparticles from Laser Ablation in Cyclopentanone and Their Embedding into a Photoresist. *Langmuir* **2010**, *26*, 6892–6897. [CrossRef]
23. Sá, S.; Silva, H.; Brandão, L.; Sousa, J.M.; Mendes, A. Catalysts for methanol steam reforming—A review. *Appl. Catal. B Environ.* **2010**, *99*, 43–57. [CrossRef]
24. Fallot, M.; Hocart, R. On the Appearance of Ferromagnetism upon Elevation of the Temperature of Iron and Rhodium. *Rev. Sci.* **1939**, *8*, 498–500.
25. Vogler, C.; Abert, C.; Bruckner, F.; Suess, D. Noise Reduction Based on an Fe−Rh Interlayer in Exchange-Coupled Heat-Assisted Recording Media. *Phys. Rev. Appl.* **2017**, *8*, 054021. [CrossRef]
26. Huang, P.-W.; Victora, R.H. Approaching the Grain-Size Limit for Jitter Using FeRh/FePt in Heat-Assisted Magnetic Recording. *IEEE Trans. Magn.* **2014**, *50*, 1–4. [CrossRef]
27. Wolloch, M.; Gruner, M.E.; Keune, W.; Mohn, P.; Redinger, J.; Hofer, F.; Suess, D.; Podloucky, R.; Landers, J.; Salamon, S.; et al. Impact of lattice dynamics on the phase stability of metamagnetic FeRh: Bulk and thin films. *Phys. Rev. B* **2016**, *94*, 174435. [CrossRef]
28. Eggert, B.; Schmeink, A.; Lill, J.; Liedke, M.; Kentsch, U.; Butterling, M.; Wagner, A.; Pascarelli, S.; Potzger, K.; Lindner, J.; et al. Magnetic response of FeRh to static and dynamic disorder. *RSC Adv.* **2020**, *10*, 14386–14395. [CrossRef]
29. Astefanoaei, I.; Gimaev, R.; Zverev, V.; Stancu, A. Modelling of working parameters of Gd and FeRh nanoparticles for magnetic hyperthermia. *Mater. Res. Express* **2019**, *6*, 125089. [CrossRef]
30. Astefanoaei, I.; Dumitru, I.; Chiriac, H.; Stancu, A. Controlling temperature in magnetic hyperthermia with low Curie temperature particles. *J. Appl. Phys.* **2014**, *115*, 17B531. [CrossRef]
31. Carrillo, P.; Shi, R.; Teeluck, K.; Senanayake, S.D.; White, M.G. In Situ Formation of FeRh Nanoalloys for Oxygenate Synthesis. *ACS Catal.* **2018**, *8*, 7279–7286. [CrossRef]
32. Meng, Y.; Gao, Y.; Li, K.; Tang, H.; Wang, Y.; Wu, Z. FeRh and Nitrogen Codoped Graphene, a Highly Efficient Bifunctional Catalyst toward Oxygen Reduction and Oxygen Evolution Reactions. *J. Phys. Chem. C* **2020**, *124*, 9142–9150. [CrossRef]
33. Swartzendruber, L.J. The Fe−Rh (Iron-Rhodium) system. *Bull. Alloy Phase Diagr.* **1984**, *5*, 456–462. [CrossRef]
34. Jia, Z.; Harrell, J.W.; Misra, R.D.K. Synthesis and magnetic properties of self-assembled FeRh nanoparticles. *Appl. Phys. Lett.* **2008**, *93*, 022504. [CrossRef]
35. Ciuculescu, D.; Amiens, C.; Respaud, M.; Falqui, A.; Lecante, P.; Benfield, R.E.; Jiang, L.; Fauth, K.; Chaudret, B. One-pot synthesis of core-shell FeRh nanoparticles. *Chem. Mater.* **2007**, *19*, 4624–4626. [CrossRef]
36. Ciuculescu, D.; Amiens, C.; Respaud, M.; Lecante, P.; Falqui, A.; Chaudret, B. Synthesis and Characterization of FeRh Nanoparticles. *Mod. Phys. Lett. B* **2007**, *21*, 1153–1159. [CrossRef]
37. Ko, H.Y.Y.; Suzuki, T. Self-assembly and magnetic properties of FePt, FeRh nanoparticles, and FePt/FeRh nanocomposite particles. *IEEE Trans. Magn.* **2007**, *43*, 885–887. [CrossRef]
38. Palmer, M.; Martinez, K.A.; Gadgil, M.G.; Campbell, D.J. Demonstrations of Magnetism and Oxidation by Combustion of Iron Supplement Tablets. *J. Chem. Educ.* **2018**, *95*, 423–427. [CrossRef]
39. Biacchi, A.J.; Schaak, R.E. The Solvent Matters: Kinetic versus Thermodynamic Shape Control in the Polyol Synthesis of Rhodium Nanoparticles. *ACS Nano* **2011**, *5*, 8089–8099. [CrossRef]

40. Ishikawa, Y.; Kawaguchi, K.; Shimizu, Y.; Sasaki, T.; Koshizaki, N. Preparation of Fe-Pt alloy particles by pulsed laser ablation in liquid medium. *Chem. Phys. Lett.* **2006**, *428*, 426–429. [CrossRef]
41. Amendola, V.; Scaramuzza, S.; Carraro, F.; Cattaruzza, E. Formation of alloy nanoparticles by laser ablation of Au/Fe multilayer films in liquid environment. *J. Colloid Interface Sci.* **2017**, *489*, 18–27. [CrossRef] [PubMed]
42. Wagener, P.; Jakobi, J.; Rehbock, C.; Chakravadhanula, V.S.K.; Thede, C.; Wiedwald, U.; Bartsch, M.; Kienle, L.; Barcikowski, S. Solvent-surface interactions control the phase structure in laser-generated iron-gold core-shell nanoparticles. *Sci. Rep.* **2016**, *6*, 23352. [CrossRef] [PubMed]
43. Amendola, V.; Scaramuzza, S.; Agnoli, S.; Granozzi, G.; Meneghetti, M.; Campo, G.; Bonanni, V.; Pineider, F.; Sangregorio, C.; Ghigna, P.; et al. Laser generation of iron-doped silver nanotruffles with magnetic and plasmonic properties. *Nano Res.* **2015**, *8*, 4007–4023. [CrossRef]
44. Amendola, V.; Riello, P.; Meneghetti, M. Magnetic Nanoparticles of Iron Carbide, Iron Oxide, Iron@Iron Oxide, and Metal Iron Synthesized by Laser Ablation in Organic Solvents. *J. Phys. Chem. C* **2011**, *115*, 5140–5146. [CrossRef]
45. Marzun, G.; Bönnemann, H.; Lehmann, C.; Spliethoff, B.; Weidenthaler, C.; Barcikowski, S. Role of Dissolved and Molecular Oxygen on Cu and PtCu Alloy Particle Structure during Laser Ablation Synthesis in Liquids. *ChemPhysChem* **2017**, *18*, 1175–1184. [CrossRef]
46. Wagener, P.; Schwenke, A.; Chichkov, B.N.; Barcikowski, S. Pulsed Laser Ablation of Zinc in Tetrahydrofuran: Bypassing the Cavitation Bubble. *J. Phys. Chem. C* **2010**, *114*, 7618–7625. [CrossRef]
47. Lim, J.; Kim, S.; Armengol, R.A.; Kasian, O.; Choi, P.; Stephenson, L.T.; Gault, B.; Scheu, C. Atomic-Scale Mapping of Impurities in Partially Reduced Hollow TiO2 Nanowires. *Angew. Chem. Int. Ed.* **2020**, *59*, 5651–5655. [CrossRef]
48. Thompson, K.; Lawrence, D.; Larson, D.; Olson, J.; Kelly, T.; Gorman, B. In situ site-specific specimen preparation for atom probe tomography. *Ultramicroscopy* **2007**, *107*, 131–139. [CrossRef]
49. Kalus, M.R.; Barsch, N.; Streubel, R.; Gokce, E.; Barcikowski, S.; Gokce, B. How persistent microbubbles shield nanoparticle productivity in laser synthesis of colloids—Quantification of their volume, dwell dynamics, and gas composition. *Phys. Chem. Chem. Phys.* **2017**, *19*, 7112–7123. [CrossRef]
50. Jung, H.J.; Choi, M.Y. Specific Solvent Produces Specific Phase Ni Nanoparticles: A Pulsed Laser Ablation in Solvents. *J. Phys. Chem. C* **2014**, *118*, 14647–14654. [CrossRef]
51. Rodríguez-Carvajal, J. Recent advances in magnetic structure determination by neutron powder diffraction. *Phys. B* **1993**, *192*, 55–69. [CrossRef]
52. Aschauer, U.J.; Braddell, R.; Brechbühl, S.A.; Derlet, P.M.; Spaldin, N.A. Strain-induced structural instability in FeRh. *Phys. Rev. B* **2016**, *94*, 014109. [CrossRef]
53. Semisalova, A. FMR Study of the Magnetic Anisotropy in Fe50Rh50 Core/Shell Nanoparticles. Master's (Diploma) Thesis, Lomonosov Moscow State University, Moscow, Russia, 2009.
54. Kuncser, V.; Rosenberg, M.; Principi, G.; Russo, U.; Hernando, A.; Navarro, E.; Filoti, G. Magnetic interactions in nanocrystalline FeRh alloys studied by in field Mössbauer spectroscopy. *J. Alloys Compd.* **2000**, *308*, 21–29. [CrossRef]
55. Filoti, G.; Kuncsea, V.; Navarro, E.; Hernando, A.; Rosenberg, M. Hyperfine fields and Fe magnetic moments in Fe-Rh alloys; a Mössbauer spectroscopy study. *J. Alloy Compd.* **1998**, *278*, 60–68. [CrossRef]
56. Trunova, A.; Lindner, J.; Meckenstock, R.; Spasova, M.; Farle, M.; Ciuculescu, D.; Amiens, C.; Chaudret, B.; Respaud, M. Temperature dependent magnetic characterisation of core/shell nanoparticles. *J. Magn. Magn. Mater.* **2009**, *321*, 3502–3506. [CrossRef]
57. Trunova, A.; Meckenstock, R.; Barsukov, I.; Hassel, C.; Margeat, O.; Spasova, M.; Lindner, J.; Farle, M. Magnetic characterization of iron nanocubes. *J. Appl. Phys.* **2008**, *104*, 093904. [CrossRef]
58. Platow, W.; Anisimov, A.N.; Farle, M.; Baberscheke, K. Magnetic Anisotropy and the Temperature Dependent Magnetic Order-Disorder Transition in Fe/Cu(001). *Phys. Status Solidi A* **1999**, *173*, 145–151. [CrossRef]
59. Sidorov, S.N.; Bronstein, L.M.; Davankov, V.A.; Tsyurupa, M.P.; Solodovnikov, S.P.; Valetsky, P.M.; Wilder, E.A.; Spontak, R.J. Cobalt Nanoparticle Formation in the Pores of Hyper-Cross-Linked Polystyrene: Control of Nanoparticle Growth and Morphology. *Chem. Mater.* **1999**, *11*, 3210–3215. [CrossRef]
60. Pang, C.P.; Hsieh, C.T.; Lue, J.T. A study of magneto-optical effect in dilute Fe3O4 ferrofluid by attenuated total reflection, ferromagnetic resonance and Faraday rotation. *J. Phys. D Appl. Phys.* **2003**, *36*, 1764–1768. [CrossRef]

61. Noginova, N.; Chen, F.; Weaver, T.; Giannelis, E.P.; Bourlinos, A.B.; Atsarkin, V.A. Magnetic resonance in nanoparticles: Between ferro- and paramagnetism. *J. Phys. Condens. Matter* **2007**, *19*, 246208. [CrossRef]
62. Antoniak, C.; Lindner, J.; Farle, M. Magnetic anisotropy and its temperature dependence in iron-rich FexPt1-x nanoparticles. *EPL Europhys. Lett.* **2005**, *70*, 250–256. [CrossRef]
63. Mancini, E.; Pressacco, F.; Haertinger, M.; Fullerton, E.E.; Suzuki, T.; Woltersdorf, G.; Back, C. Magnetic phase transition in iron-rhodium thin films probed by ferromagnetic resonance. *J. Phys. D Appl. Phys.* **2013**, *46*, 245302. [CrossRef]
64. Merkel, D.G.; Lengyel, A.; Nagy, D.L.; Németh, A.; Horváth, Z.E.; Bogdán, C.; Gracheva, M.A.; Hegedűs, G.; Sajti, S.; Radnóczi, G.Z.; et al. Reversible control of magnetism in FeRh thin films. *Sci. Rep.* **2020**, *10*, 13923. [CrossRef] [PubMed]
65. Zingsem, B.W.; Feggeler, T.; Terwey, A.; Ghaisari, S.; Spoddig, D.; Faivre, D.; Meckenstock, R.; Farle, M.; Winklhofer, M. Biologically encoded magnonics. *Nat. Commun.* **2019**, *10*, 4345. [CrossRef]
66. Stashkevich, A.A.; Roussigneé, Y.; Djemia, P.; Billet, D.; Stognij, A.I.; Novitskii, N.N.; Wurtz, G.; Zayats, A.V.; Viau, G.; Chaboussant, G.; et al. Brillouin light scattering observation of the transition from the superparamagnetic to the superferromagnetic state in nanogranular (SiO_2)Co films. *J. Appl. Phys.* **2008**, *104*, 93912. [CrossRef]
67. Voronin, D.V.; Sadovnikov, A.V.; Shchukin, D.G.; Gorin, D.A.; Beginin, E.N.; Sharaevskii, Y.P.; Nikitov, S.A. Studying the spectra of thermal magnons in composite materials with embedded magnetite nanoparticles using Brillouin light-scattering spectroscopy. *Tech. Phys. Lett.* **2013**, *39*, 715–718. [CrossRef]
68. Lu, H.; Liang, F.; Gou, J. Nanopaper enabled shape-memory nanocomposite with vertically aligned nickel nanostrand: Controlled synthesis and electrical actuation. *Soft Matter* **2011**, *7*, 7416–7423. [CrossRef]

DOI: 10.3390/nano10122362
URN: urn:nbn:de:hbz:464-20210211-123007-1